Joule

Article

# Scalable and sustainable manufacturing of twin boundary-enhanced flexible $Bi_{0.4}Sb_{1.6}Te_3$ films with high thermoelectric performance

## Graphical abstract

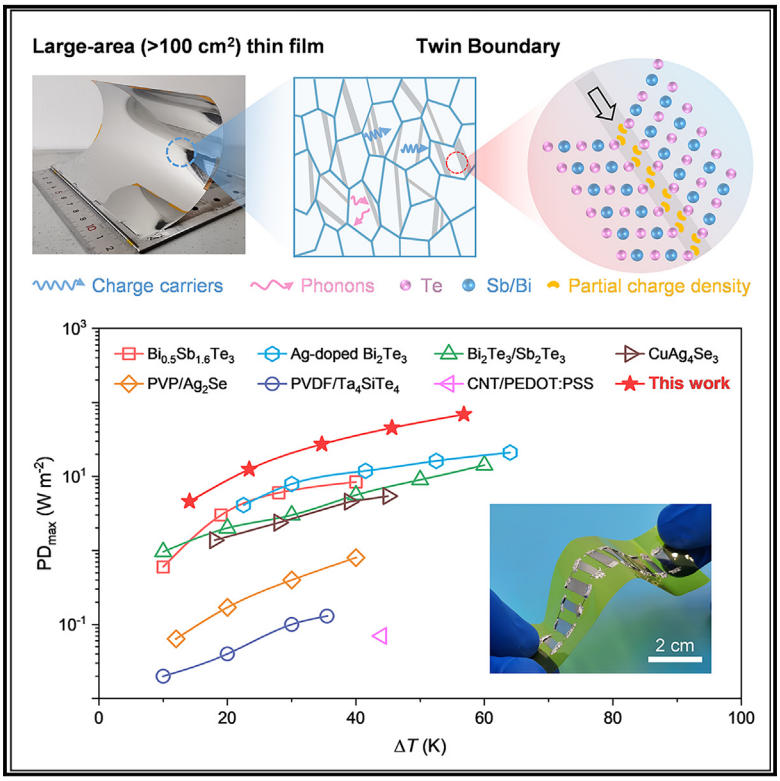


## Highlights

- Twin boundary-boosted power factor of 45 μW $cm^{-1}$ $K^{-2}$ and ZT of 1.4 at room temperature
- The high density of twins promotes local strain propagation toward enhanced flexibility
- A flexible TE generator enables to generate a power density of 69 W $m^{-2}$ at $\Delta T$ = 56.8 K
- A large-area, cost-effective $Bi_{0.4}Sb_{1.6}Te_3$ thin film of up to 100 $cm^2$ is developed

## Authors

Dasha Mao, Yi Zhou, Yong Yu, ..., Lin Xie, Ghim Wei Ho, Jiaqing He

## Correspondence

hejq@sustech.edu.cn

## In brief

A high density of annealing twin boundaries is demonstrated to simultaneously modulate the carrier concentration, Seebeck coefficient, mobility, and local strain propagation. These results lead to ultrahigh thermoelectric (TE) performance at room temperature and high flexibility. Additionally, a flexible TE generator achieved an impressive power density guided by finite-element modeling. More importantly, the developed $Bi_{0.4}Sb_{1.6}Te_3$ films demonstrate low electricity consumption and carbon footprint, offering a new avenue for large-scale (>100 $cm^2$) and sustainable manufacturing.

Mao et al., 2024, Joule *8*, 3313–3323
December 18, 2024 
https://doi.org/10.1016/j.joule.2024.08.009

CellPress

Joule

CellPress

Article

# Scalable and sustainable manufacturing of twin boundary-enhanced flexible $Bi_{0.4}Sb_{1.6}Te_3$ films with high thermoelectric performance

Dasha Mao,[1,5] Yi Zhou,[2,5] Yong Yu,[1] Yan Wang,[1] Meng Han,[3] Qiyu Meng,[1] Yao Lu,[1] Jianghe Feng,[1,3] Minghua Kong,[1] Hailong Yang,[1] Quan Gan,[1] Xiao Xu,[1] Lin Xie,[1] Ghim Wei Ho,[2] and Jiaqing He[1,4,6,*]

[1]Shenzhen Key Laboratory of Thermoelectric Materials, Department of Physics, Southern University of Science and Technology, Shenzhen 518055, China

[2]Department of Electrical and Computer Engineering, National University of Singapore, Singapore 117581, Singapore

[3]Shenzhen Institute of Advanced Electronic Materials, Shenzhen Institute of Advanced Technology, Chinese Academy of Sciences, Shenzhen 518055, China

[4]Guangdong Provincial Key Laboratory of Advanced Thermoelectric Materials and Device Physics, Southern University of Science and Technology, Shenzhen 518055, China

[5]These authors contributed equally

[6]Lead contact

*Correspondence: hejq@sustech.edu.cn

https://doi.org/10.1016/j.joule.2024.08.009

**CONTEXT & SCALE** Thermoelectric (TE) technology can directly convert heat to electricity, providing a vast possibility for waste heat recovery toward energy sustainability and carbon neutrality. However, flexible TEs are limited by the low power factor (PF) and brittleness of materials, especially at room temperature. In this study, uniformly distributed twins were found to simultaneously modulate the carrier concentration, Seebeck coefficient, mobility, and local strain propagation in the film, resulting in superior TE performance and enhanced flexibility at room temperature. Additionally, guided by finite-element modeling, an impressive maximum power density of 69 W $m^{-2}$ under a temperature difference of 56.8 K was achieved using a flexible TE generator. This breakthrough offers a practical blueprint for wearable electronics and sustainable heat harvesting.

## SUMMARY

Flexible thermoelectrics (TEs) have been used in self-powered electronics and heat harvesters due to their matchable heat flux values across curved/non-flat interfaces, aiming to achieve a balance between thermoelectricity, flexibility, and scalability. In this work, we constructed $Bi_{0.4}Sb_{1.6}Te_3$ thin films with a high density of annealing twin boundaries to simultaneously modulate the carrier concentration, Seebeck coefficient, mobility, and local strain propagation. Specifically, the thin films achieved an ultrahigh power factor reaching 45 μW $cm^{-1}$ $K^{-2}$ and demonstrated modest electrical conductivity variations (<10%) after 1,000 bending cycles at room temperature. Furthermore, we presented a large-area, cost-effective thin film of up to 100 $cm^2$ and a flexible generator with an impressive maximum power density of 69 W $m^{-2}$ at a temperature difference of 56.8 K. This flexible TE could not only serve as a framework for comprehending the structure-property correlation in inorganic TE thin films but also provide feasibility for wearable electronics and sustainable heat harvesting.

## INTRODUCTION

Thermoelectric (TE) technology enables direct energy conversion between heat and electricity, providing waste heat recovery for energy sustainability and net zero carbon emissions.[1–3] The TE performance of materials is typically determined by the dimensionless figure of merit (ZT) according to $ZT = S^2\sigma T/\kappa_{tot}$, where $S$ is the Seebeck coefficient, $\sigma$ is the electrical conductivity, $T$ is the absolute temperature, and $\kappa_{tot}$ is the total thermal conductivity.[4–6] However, the interplay between these intrinsic parameters ($S$, $\sigma$, and $\kappa_{tot}$) and the effective mass ($m^*$) alongside carrier concentration ($n$) (e.g., $S \propto m^*$, $\sigma \propto 1/m^*$, $S \propto n^{-2/3}$, and $\sigma \propto n$) makes ultrahigh $ZT$ challenging, especially for $Bi_2Te_3$-based TE materials at ambient temperature. Therefore, considering

low-grade heat harvesting at non-flat or curved surfaces, the minimization of heat loss across heterointerfaces necessitates a concise balance between high thermoelectricity and flexibility to achieve cost-effectiveness and sustainability demands. Recently, high TE performance and mechanical properties have been obtained in $Bi_2Te_3$-based bulk materials. The transformation of innate rigidity and brittleness into highly flexible thin films has attracted attention from academia and industry. For example, physical vapor deposition techniques such as magnetron sputtering (MS), vacuum thermal evaporation (VTE), pulsed laser deposition (PLD), and molecular beam epitaxy (MBE)[7–14] have been implemented, yielding dense and high-performance inorganic TE thin films. Specifically, Zheng et al.[12] reported on an Ag-doped $Bi_2Te_3$ flexible film with (*000l*) orientation, where the thermal and electrical transport properties at the in-plane direction were optimized through the introduction of Ag multiple defects. Similarly, a strong (00*l*)-orientation $Ag_2Se$ thin film was assessed by lowering the (00*l*) formation energy due to the defects of tellurium (Te) occupancy at the Se position.[13] Fu et al.[14] prepared a high-quality $Bi_{0.5}Sb_{1.5}Te_3$ van der Waals epitaxy film on a sapphire substrate grown using PLD, which exhibited a high in-plane *ZT* value of ~0.9. However, the underlying mechanism of electrothermal transport in $Bi_2Te_3$-based TE thin films has rarely been assessed and fully elucidated. Moreover, in $Bi_2Te_3$-based polycrystalline thin films, TE transport is sophisticated and typically involves multiple competitive mechanisms.

Interestingly, grain boundary (GB) scattering has been shown to manipulate mass (atoms), heat (phonons), and charge (carriers) transport in bulk TE materials recently.[15] The presence of GBs can lead to incomplete atomic bonds at interfaces, effectively modulating the carrier concentration while impeding inter-grain carrier movement due to energy barriers.[16–18] More importantly, compared with GB structures, twin boundaries (TBs) often possess low energy and typically form a stable, coherent interface.[19] For example, Biswas et al.[20] reported that the integration of coherent interfaces into PbTe-based bulk materials could mitigate carrier scattering without lowering the carrier mobility, allowing for a large power factor (PF) of 25 $\mu W\ cm^{-1}\ K^{-2}$. Therefore, a comprehensive understanding of the impact of TB engineering on the electrical transport mechanism is critical for enhancing TE properties. In $Bi_2Te_3$-based materials with a rhombohedral *R-3m* space group and quintuple layers (QLs, Te(1)-Sb/Bi-Te(2)-Sb/Bi-Te(1)), van der Waals forces (the weakest in this structure[7,21]) dominate the interactions between neighboring QLs along the c axis direction.[22] Consequently, layered bulk materials are likely to experience slippage and deformation along the (*000l*) crystal plane under thermal stress, ball milling, or annealing processes, resulting in the formation of deformation twins.[23–25] Fortunately, TB can maintain a bulk-like atomic arrangement, potentially facilitating favorable carrier transport properties.[26] For example, Yu et al.[27] demonstrated that numerous TBs in a $Bi_{0.5}Sb_{1.5}Te_3$ bulk system obtained using liquid-state manipulation methods could filter low-energy carriers to achieve a large Seebeck coefficient of 217 $\mu V\ K^{-1}$ at room temperature. Mao et al.[28] discovered an abundance of nanoscale twins in Cu-Ni alloys, which significantly improved the TE performance by 34% at 873 K. Nevertheless, the nanosized grains and micro-nanometer film thickness made it challenging to introduce deformation twins via dynamic plastic deformation.[29] Further, high-density annealing twins have been successfully introduced through heat treatment. However, few studies have investigated how the formation and manipulation of twin structures impact the thermoelectricity and flexibility of inorganic thin films, especially at ambient temperature.

In this work, inspired by the electrical transport mechanism of bulk polycrystalline, we presented a novel flexible $Bi_{0.4}Sb_{1.6}Te_3$ (BST) film obtained using the VTE method alongside an optimized thermal annealing process. Notably, the uniformly distributed TBs were found to selectively restrain phonon propagation while promoting carrier transport in the film. In addition, the introduced density of state (DOS) significantly enhanced the Seebeck coefficient to ~180 $\mu V\ K^{-1}$ with negligible electrical conductivity deterioration (Figure 1A). Consequently, a synergistic combination of a high Seebeck coefficient and superior electrical performance resulted in an impressive PF of 45 $\mu W\ cm^{-1}\ K^{-2}$ and a *ZT* value of ~1.4 at room temperature, outperforming other TE thin films (Figure 1B).[9,14,30–34] Our experimental and computational results demonstrated that TBs played a pivotal role in striking a balance between the characteristics of carrier transport, TE performance, and flexibility. We also constructed a flexible TE generator (f-TEG) with a power density of 69 $W\ m^{-2}$ under a temperature difference of 56.8 K, which was highly competitive with reported in-plane TE devices (Figure 1C).[10,12,31,33,35–38] This approach meticulously optimizes the arrangement and density of TBs within the polycrystalline flexible thin film, introducing a new dimension to TE performance improvement and offering a refined control over flexibility and thermal management. This finding may serve as an exemplary framework for understanding the structure-property relationships of inorganic flexible TE thin films.

## RESULTS

### Microstructure and characterization of BST thin films

BST thin films were initially deposited on flexible polyimide (PI) substrates using VTE and subsequently annealed at temperatures ranging from 323 to 673 K, with increments of 50 K. The surface morphology of the films is shown in Figure S1, which reveals that the samples possessed a dense and smooth surface. Notably, during the annealing process, the BST grains merged with one another, leading to recrystallization and expansion in the size of tens of nm to several hundreds of nm. Additionally, the surface roughness of the annealed films was ~10 nm, which was sufficiently low and considered nearly flat (Figure S2). In the VTE method, the thicknesses at each location in the deposited films were precisely manipulated using crystal detectors, achieving a high degree of concordance with the measurements obtained from a step profiler and via cross-sectional scanning electron microscopy (SEM) (Figure S3). Energy dispersive spectroscopy (EDS) analysis revealed that Te, antimony (Sb), and bismuth (Bi) atoms were evenly distributed across the film surface (Figure S4). This uniform distribution suggested no precipitation of the secondary phases before or after the annealing process, confirming that the p type BST thin film maintained a homogeneous composition.

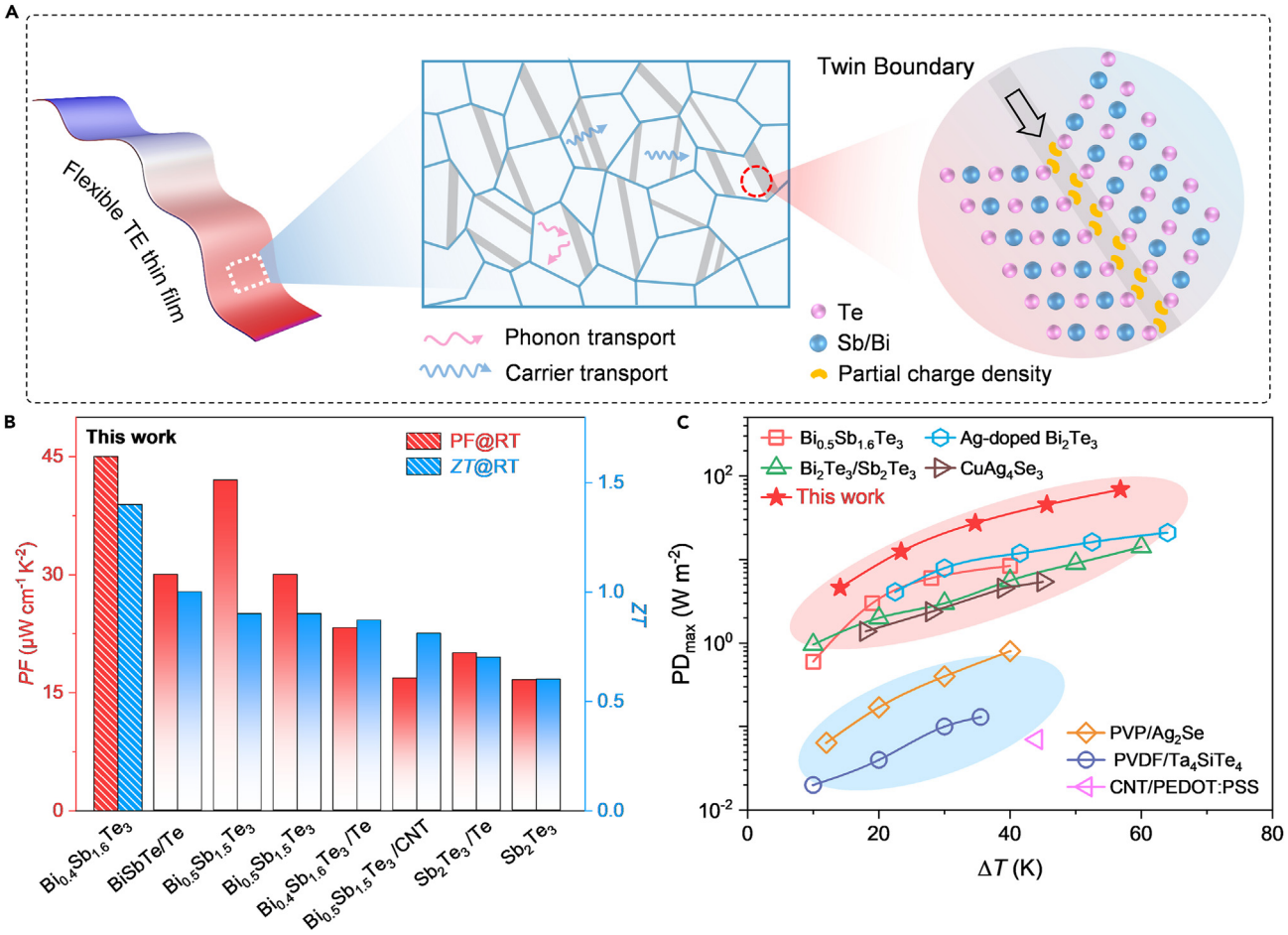


**Figure 1. Twin boundaries enhanced the flexible $Bi_{0.4}Sb_{1.6}Te_3$ thin film with ultrahigh TE performance**

(A) Schematic diagram of the flexible p type $Bi_{0.4}Sb_{1.6}Te_3$ thin film, with detailed insets highlighting the carrier and phonon transport mechanisms, the structure of the twin boundaries, and a conceptual depiction of the partial charge density situated between the Te(1)-Te(1) atomic layers.

(B) State-of-the-art comparison of TE performance at room temperature for p type flexible $Bi_2Te_3$-based films.[9,14,30–34]

(C) Comparison of maximum output power density ($PD_{max}$) versus temperature difference revealed that the obtained $PD_{max}$ was higher than the f-TEGs with TE strips fabricated using similar PVD techniques (light red)[10,12,31,33,35] and conventional chemical approaches (light blue).[36–38]

The Euler map (Figure 2A) and GB statistics (Figures 2B and 2C) derived from electron backscatter diffraction (EBSD) provided crucial insights into the microstructure of BST thin films after annealing at 623 K for 2 h. EBSD analysis demonstrated an average grain size of ~800 nm with a relatively uniform pattern. The central region of the pole figure (Figure S5) exhibited a lighter hue, while a surrounding circle was darker, indicating that the majority of grains inclined at certain angles relative to the transverse direction-rolling direction (TD-RD) coordinate system but tended to form a (*000l*) texture. Moreover, the X-ray diffraction (XRD) results (Figure S6) of the films subjected to various annealing treatments revealed improved crystallinity, and a more pronounced (*000l*) peak could be attributed to a higher annealing temperature, suggesting preferential grain growth along the (*000l*) plane. The orientation factor value of the (*000l*) crystal plane in the films annealed at 623 K was 0.351, with the details provided in Note S1. The GB map in Figure 2B illustrated three categories of GBs, namely, high-angle GBs (HAGBs) ranging from 15° to 110°, low-angle GBs (LAGBs) between 5° and 15°, and TBs with a typical misorientation angle of 60° ± 2°, as reported in previous studies.[27,39] Furthermore, as shown in Figure 2C, misorientation angle statistics indicated that over 90% of the GBs were HAGB. Notably, the 60° misorientation angle was particularly prominent, encompassing not only the conventional 60° GBs (blue histogram) but also the majority of TBs (red histogram), accounting for ~25.2% of the total GB length. EBSD statistical analysis verified that the TB was minimal in the films annealed at 423 and 473 K (Figure S7), while a significant increase was observed at 623 K, resulting in coherent twins (denoted as TB-rich BST thin films, Figure S8 and Note S2).

To investigate the impact of twinning on the TE properties, BST thin films with high crystallinity were prepared through *in situ* deposition at 623 K, denoted as TB-poor BST thin films, which exhibited lower twinning content versus their annealed counterparts. Statistically, the TB-poor BST thin film had a smaller grain size but showed similar crystallographic orientation

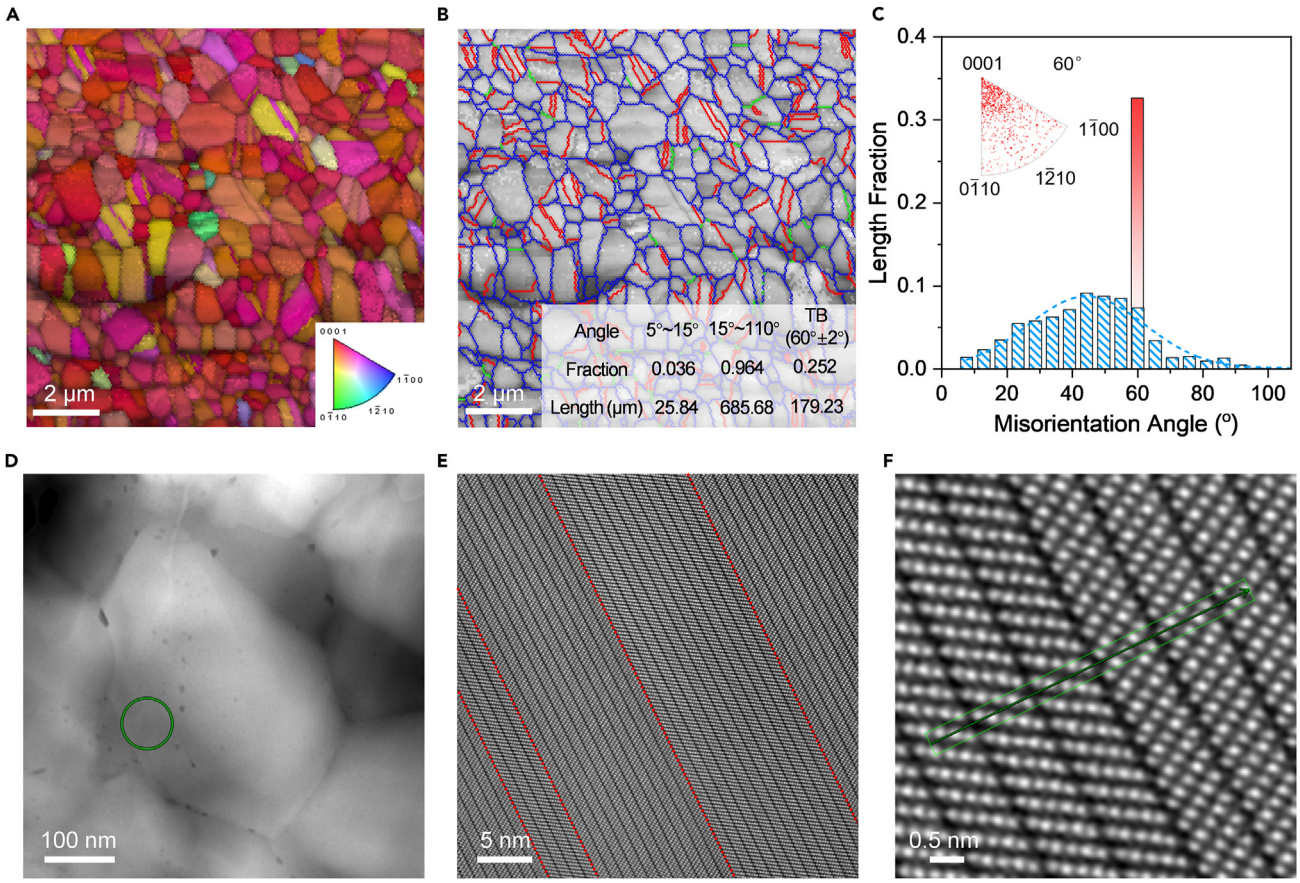


**Figure 2. Microstructure and characterization of the $Bi_{0.4}Sb_{1.6}Te_3$ thin films**

(A) Euler map of the in-plane EBSD images of the TB-rich BST thin film.

(B) Image quality (IQ) corresponds to (A), where the blue lines represent the HAGB, the green lines represent the LAGB, and the red lines represent the TB. The inset chart represents the statistical results derived from various boundaries.

(C) Quantitative statistics of various types of GBs, revealing that the distribution of conventional GBs (depicted by the blue histogram) followed a normal distribution, while the protrusion at 60° (depicted by the red histogram) corresponded to additional fractions occupied by TBs. The inset image illustrates that the majority of the 60° GBs had a propensity to align with the (*000l*) plane.

(D and E) Low-magnification TEM image (D), as well as (E) high-magnification TEM image of area within the green circle in (D), and TBs marked by red lines.

(F) Atomically resolved STEM-HAADF images, showing a highly symmetrical twin interface structure. The corresponding atomic intensity curve for the green lines is shown in Figure S11B.

growth with the TB-rich BST samples (Figures S9 and S10). However, the twinning length per unit area in the TB-rich BST thin films was more than 7-fold greater than the TB-poor sample, and the area ratio of twins in the TB-rich sample was 57.6%, in contrast to just 10% in the TB-poor sample (Figure S11 and Note S3). This clearly illustrates the high density of twinning in the TB-rich sample. As observed through in-plane scanning transmission electron microscopy (STEM) characterization of the TB-rich sample, the low-magnification image confirmed that the grain size was consistent with the SEM and EBSD data (Figure 2D). However, due to the inherently small grain size, TBs were not apparent. The higher-magnification image revealed the presence of distinct annealing twins, and several parallel TBs were observed within a single grain (Figures 2E and 2F). The fast Fourier transform (FFT) pattern corresponding to Figure 2E demonstrated two sets of symmetrical crystal planes (Figure S12A). The intensity profiles along the green line region in Figure 2F (Figure S12B) revealed that Te(1)-Te(1) spacing between the TBs and the general van der Waals layer was virtually identical at ~280 pm. These results served as a foundation for the proposed twin structure model, and the examination of atomic arrangement in the high-magnification image showed that the atoms within the grains were organized with a characteristic QL pattern (Figure S12C).

## TE properties and carrier transport mechanisms

The annealing process was found to play a pivotal role in the TE performance of the BST thin films. Following an optimization of thickness, 1-μm film was chosen for further investigation (Figure S13). Figure S14 summarizes the TE performance of the BST thin films at different annealing temperatures. These results indicated that the electrical conductivity of the films improved with increasing annealing temperatures, especially above 473 K, while the Seebeck coefficient slightly decreased. This was

ascribed to a combination of factors, including grain growth, improved crystallinity, and enhanced texture of the films (Figures S1 and S6). This also led to a significant increase in the PF of 45 μW cm$^{-1}$ K$^{-2}$ at room temperature after annealing at a temperature of 623 K. More importantly, carrier scattering in the films was dominated by acoustic phonons when the annealing temperature exceeded 473 K, according to the mobility variations across the different samples (Figures S14E and S14F). These findings not only contributed to high electrical performance but also facilitated the Seebeck coefficient increase by ~700% over the pristine film. Structural analysis also suggested that these films contained a high density of TBs (Figure 2). Consequently, to investigate the effect of annealing TBs on the TE performance of the films, we introduced *in situ* annealed TB-poor thin films with a reduced concentration of TBs for comparison. Figures 3A and 3B present the TE performance of the two types of thin films as a function of temperature. Both thin films exhibited excellent electrical properties, and the trend of conductivity decrease with increasing temperature was consistent with the transport behavior of degenerate semiconductors. However, the TB-rich film showed a significantly higher Seebeck coefficient than the TB-poor film, providing an average PF of 33.7 μW cm$^{-1}$ K$^{-2}$ ($300 \leq T \leq 453$ K), which surpassed that of the TB-poor films (22.9 μW cm$^{-1}$ K$^{-2}$) and other p-type thin films (Table S1).[9,14,31,32,40] Moreover, three high-to-low temperature testing cycles were conducted on the TB-rich and TB-poor films, demonstrating their excellent stability and durability (Figure S15). Concurrently, the evaluation of samples from distinct batches further highlights the dependable repeatability of the production process (Figure S16). To explain the differences in electrical conductivity and Seebeck coefficient between the two films, carrier concentration and mobility characterization were performed (Figure 3C). The TB-rich BST film demonstrated higher carrier mobility than the TB-poor thin films, suggesting a concurrent reduction in carrier concentration. This is because the TBs exhibited weaker interfacial scattering than other general interfaces, allowing the carriers to traverse these boundaries without the mobility decline typically associated with strong interface filtering, which can be verified by the gradual disappearance of the potential barrier height in Figure S14F. Furthermore, the carrier concentration and mobility of the TB-rich and TB-poor thin films were found to follow the temperature dependence of $T^{-r}$ ($1.0 \leq r \leq 1.5$), demonstrating that acoustic phonon scattering was the predominant mechanism affecting these properties, and this behavior aligned with the single parabolic band (SPB) model[16] (Note S4). Therefore, the effective mass values of the two thin films were deduced from the *S* and *n* relationship. Compared with other recently reported p-type $Bi_2Te_3$-based thin films (Figure 3D),[9,14,30,32,34] it was evident that the reduced carrier concentration and increase in $m^*$ from $0.8m_0$ (TB-poor) to $1.03m_0$ (TB-rich) enhanced the Seebeck coefficient.

To explore the underlying mechanism of electrical transport in depth, ultraviolet photoelectron spectroscopy (UPS) characterization was performed on the TB-rich and poor BST thin films, and we calculated the energy band structures and DOS for scenarios with and without twins. Figure 4A shows the secondary electron cutoff region, which was indicative of the work function (WF), as well as the onset of the valence band (VB) region, and a Tauc plot representation of the band gap is shown in Figure S17. According to UPS analysis, WF increased from −3.95 eV (TB-poor) to −4.12 eV (TB-rich), and the fermi level of the TB-rich sample was positioned closer to the center of the band gap than the fermi level of the TB-poor sample (Figure 4B). This observation suggested that the increment of TB content in the films was beneficial for transitioning from strong p-type (TB-poor BST film) to weak p-type (TB-rich BST film) semiconductor behavior. Concurrently, this points to an increase in the population of electrons occupying the energy bands, which accounted for the lower carrier concentration in the TB-rich BST thin films. Additionally, to elucidate the change in energy band structure, we performed theoretical calculations on systems with and without TB (Figure 4C), utilizing the established twin model (Figure S12 and Note S5). We observed that the incorporation of TB moved the fermi level toward the conduction band. This shift functioned analogously to donor doping, supplying electrons that compensated the hole carriers in the p-type thin films, resulting in a decrease in carrier concentration. We experimentally determined the energy-level diagrams of the TB-rich and TB-poor BST thin films, which were corroborated by the results obtained from the theoretical calculations. Furthermore, the effective mass of the hole carriers was contingent upon the gradient of the valence band maximum (VBM). The expression for the effective mass derived from the DOSs is shown in Equation 1 [41]:

$$DOS(E) = \frac{1}{2\pi^2}\left(\frac{2m_d^*}{\hbar^2}\right)^{\frac{3}{2}} E^{\frac{1}{2}}. \qquad \text{(Equation 1)}$$

Figure 4C reveals the significant increase in the slope of the TB-rich BST thin film near the VBM. Combined with the above formula, it was evident that the twin structure endowed the film samples with a higher DOS and effective mass than structures devoid of twins, aligning with the experimental observations. The plane-average difference charge density also revealed an additional DOS within the Te(1)-Te(1) layer near the TB in real space (Figures 4D and S18), which was likely responsible for the increase in DOS induced by the TBs. The cumulative effect of all the aforementioned factors contributes to the enhancement in the Seebeck coefficient in the TB-rich BST thin film.

In addition, for TE materials and devices, the thermal conductivity and power density can be characterized in both out-of-plane and in-plane directions, as long as the thermal and electrical measurements are conducted along the same direction, as illustrated in Figure S19. Here, the in-plane thermal transport properties of both films at room temperature were evaluated using a transient-photo-electro-thermal (TPET) method[42] (Figure S20 and Note S6), yielding thermal conductivities of 1.05 W m$^{-1}$ K$^{-1}$ for the TB-poor BST thin film and 0.95 W m$^{-1}$ K$^{-1}$ for the TB-rich BST thin film (Table S2). The observed reduction in thermal conductivity can be linked to the presence of TBs,[43] which are estimated to contribute ~24% to phonon scattering. Further analysis using the Debye-Callaway model, as depicted in Figure S20D and Note S7 (with specific parameters outlined in Table S3), indicates

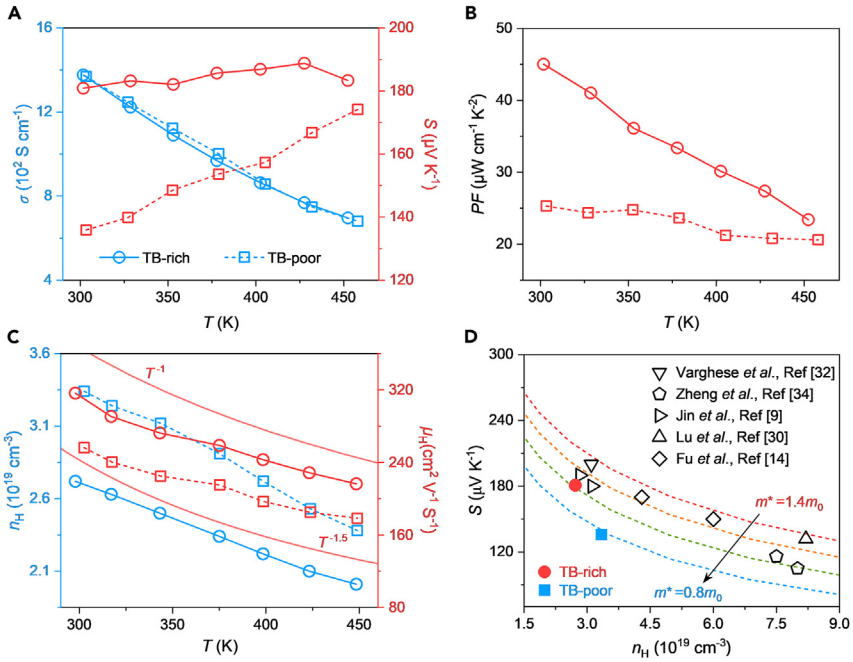


**Figure 3. TE performances and carrier transport mechanisms of the $Bi_{0.4}Sb_{1.6}Te_3$ thin films**

(A and B) The temperature-dependent TE performances of (A) electrical conductivity, Seebeck coefficient, as well as (B) the power factor of the TB-rich and TB-poor BST thin films.

(C) The carrier concentration and mobility of the BST thin films.

(D) The carrier density-dependent values of *S* of the BST thin films and reported $Bi_2Te_3$-based films.[9,14,30,32,34] The dashed lines were calculated by the single parabolic band (SPB) model, where $m^*$ denotes the effective mass.

that TBs effectively scatter mid- to low-frequency phonons. This brings forth a subsequent decrease in lattice thermal conductivity, aligning closely with the experimental findings. Consequently, a *ZT* value of ~1.4 of TB-rich BST thin films was obtained at room temperature, which was competitive among state-of-the-art p-type $Bi_2Te_3$-based thin films.

## Flexibility, scalability, and sustainability of the BST thin films

In terms of the QL structure, the texture of the grains could theoretically promote the flexibility of the film when the bending plane was parallel to these layers due to the interlayer separation/slip of the (0001)<$\bar{1}2\bar{1}0$> slip systems.[44] However, in polycrystalline thin films under deformation, conventional GBs have often shown an insufficient ability to accumulate dislocations, leading to unstable flexibility and toughness, with the TBs providing sufficient space for dislocation accumulation and storage.[45] To better elucidate the mechanism, the deformation behavior (Figure S21) of the TB structure was represented by molecular dynamics (MD) simulations. Observations revealed that the symmetry of atomic displacements within the grains was preserved along the y axis during bending deformation, irrespective of the presence of TB. However, in the z axis direction, grains with TB displayed a consistently symmetric distribution of atomic displacements aligned with the TB, while those without TB showed asymmetry and instability in their displacement patterns (Figure 5A; Video S1). These findings indicated that the bending strain was effectively distributed and accommodated along the TB. From the perspective of tensile deformation, we observed that dislocations traversed across the TB, entering the twin lamellae and assimilating into the coherent TB. The dislocations then dissociated into distinct partial dislocations, gliding along the TB or forming dislocation locks near the TB (Figure S22; Videos S2 and S3). This ensured that the material maintained superior structural integrity during deformation under external stress, significantly reducing the propensity for fracture and averting serious degradation of its electrical properties.[48,49] Guided by MD simulation guidance, TB-rich, TB-poor, and pristine BST films with a thickness of ~1 μm were utilized for flexibility testing (Figure 5B; Video S4). Notably, at a bending radius of 5.0 mm, the electricity conductivity of the TB-rich BST film was maintained at ~91% of $\sigma_0$ after 1,000 bending cycles, while ~85% and ~74% of $\sigma_0$ remained for the TB-poor and pristine BST films, respectively. A significant drop in film electricity occurred when the bending radius was reduced below 3 mm, signaling that the film had reached its bending limit in practical applications. The calculated mechanical strain for the TB-rich film at this point is ~0.6%, whereas the ultimate strain for the TB-poor film is 0.4% (Note S8). Consequently, it can be deduced that a high density of nanoscale twins enabled the effective transmission of localized stresses, enhancing material strength without compromising its flexibility. Based on these findings, the substantial increase in flexibility of the thin film also endowed f-TEG with exceptional flexibility (Figure 5C). The $\sigma/\sigma_0$ remained over 90% for the minimally encapsulated prototype consisting of a single pair of p-n legs (the TE performance of n-leg is detailed in Table S4) after 1,000 bending cycles (*r* = 10, 15, and 20 mm) in both horizontal and vertical directions (Figure S23), presenting its distinct mechanical. For f-TEG, the relationship between the electrical output and its geometry is analyzed using finite-element simulation (Figure 5D) in conjunction with a homemade test platform (Figure S24) for evaluating device performance. Numerically, at the temperature difference of $\Delta T$ = 56.8 K, the $PD_{max}$ of 75 W $m^{-2}$ was obtained when the cross-sectional area ratio between p- and n-type f-TE strips ($A_p/A_n$) is maintained at 0.7 and *L* = 10 mm. When the temperature difference between the hot end and the cold end is kept at 56.8 K, the measured open circuit voltage is 132.9 mV, which is consistent with the results calculated according to the equation $V_0 = N \cdot S_{np} \cdot (T_h - T_c)$ (Figure S25 and Note S9). In addition, the contact resistance ($R_C$) between the electrode and the TE film is relatively low (Figure S26) and negligible. The maximum output power could be

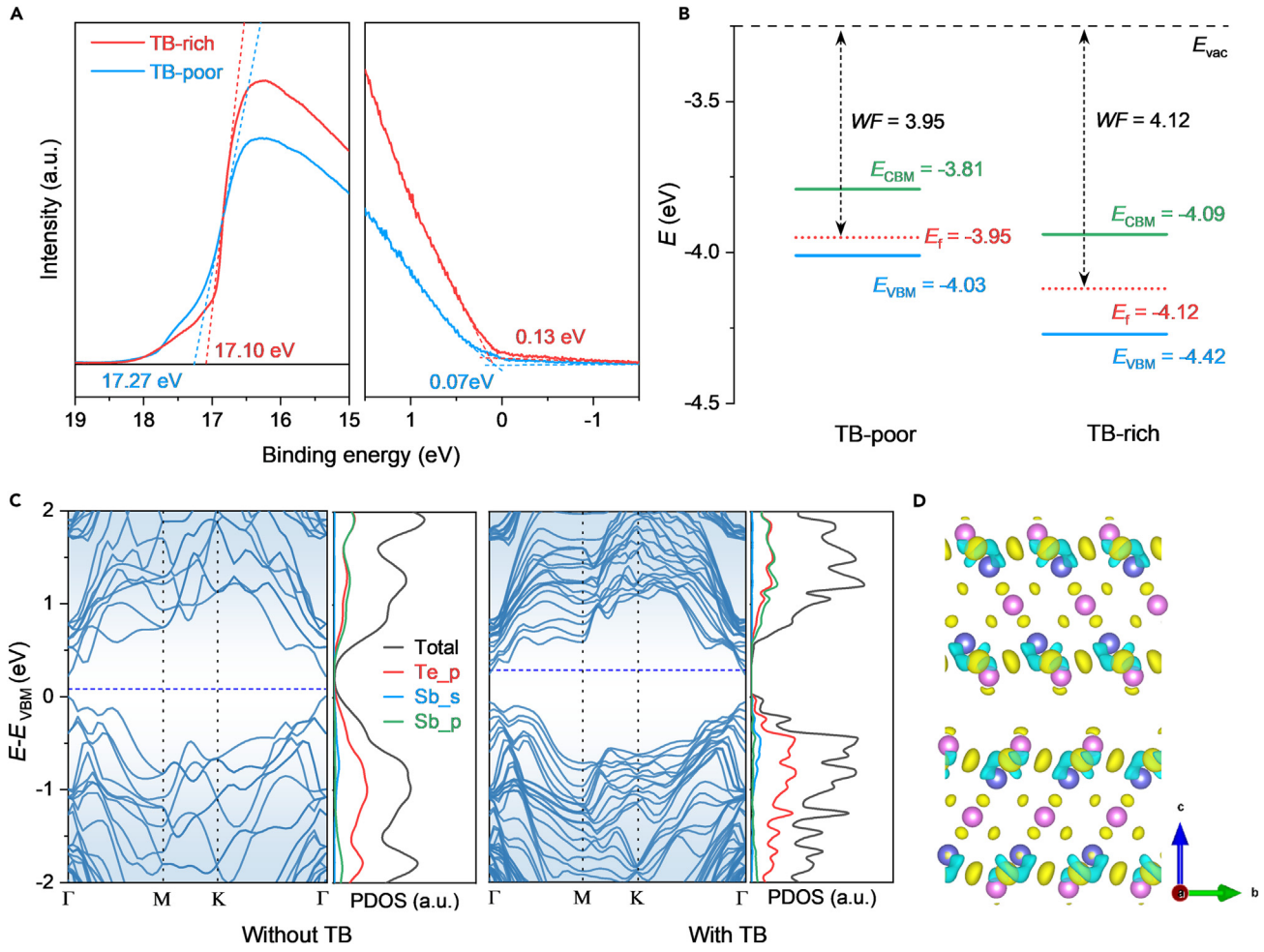


**Figure 4. Band structures for the $Bi_{0.4}Sb_{1.6}Te_3$ thin films**

(A) Secondary electron cutoff spectra (left), as well as (right) valence band (VB) structure.

(B) Experimentally determined energy-level diagrams of the TB-rich and TB-poor BST thin films from ultraviolet photoelectron spectroscopy (UPS) studies.

(C) Calculated electronic band structure and projected density of states (PDOSs) of $Sb_2Te_3$ supercells (left) without and (right) with TB according to density functional theory (DFT) simulations.

(D) Partial plane-average difference charge density of the TB model, showing additional DOS between the Te(1)-Te(1) atomic layers in the TB.

obtained when a load resistance ($R_l$) is equal to the internal resistance ($R_{in}$) of the device. Consequently, it can be inferred that $R_{in}$ of the device is ~200 Ω, and the $P_{max}$ under the temperature difference of 56.8 K was 21 μW (Figure 5E). Additional calculations yielded a $PD_{max}$ value of 69 W $m^{-2}$ for the f-TEG, which closely aligned with the predicted value. To demonstrate the feasibility of sustainable and scalable manufacturing of the proposed BST thin films, functional f-TEG fabrication was conducted under physics-guided co-design (Figure 5F).[47] Notably, the deposited large-scale (>100 $cm^2$, Figure S27) and uniform film demonstrated lower electricity consumption and carbon footprint toward sustainable development compared with other techniques (Table 1). Following the assessment of sustainable performance from materials to devices, we compared our findings with a selection of emblematic reports and demonstrated superiority in both energy conservation and sustainable large-scale production (Figure 5G).[9,12,46] Compared with the majority of advanced f-TEGs, our device also had significant advantages (Table S5).[33,34,36,37,50,51]

## DISCUSSION

In summary, in this work, we prepared an ultrahigh TE performance flexible BST film with high-density annealing TBs using the VTE method. The incorporation of twins in the BST thin films fine-tuned the carrier concentration range and augmented the effective mass, leading to an increase in the Seebeck coefficient by ~30% in the TB-rich sample compared with the TB-poor sample. Moreover, the weaker scattering effect at the TBs than at conventional GBs preserved high carrier mobility by allowing energetic carriers to pass through unimpeded, resulting in an excellent PF of 45 μW $cm^{-1}$ $K^{-2}$. Additionally, the TBs and their stress fields intensified phonon scattering, leading to a reduction in thermal conductivity and a high $ZT$ value of ~1.4 at room

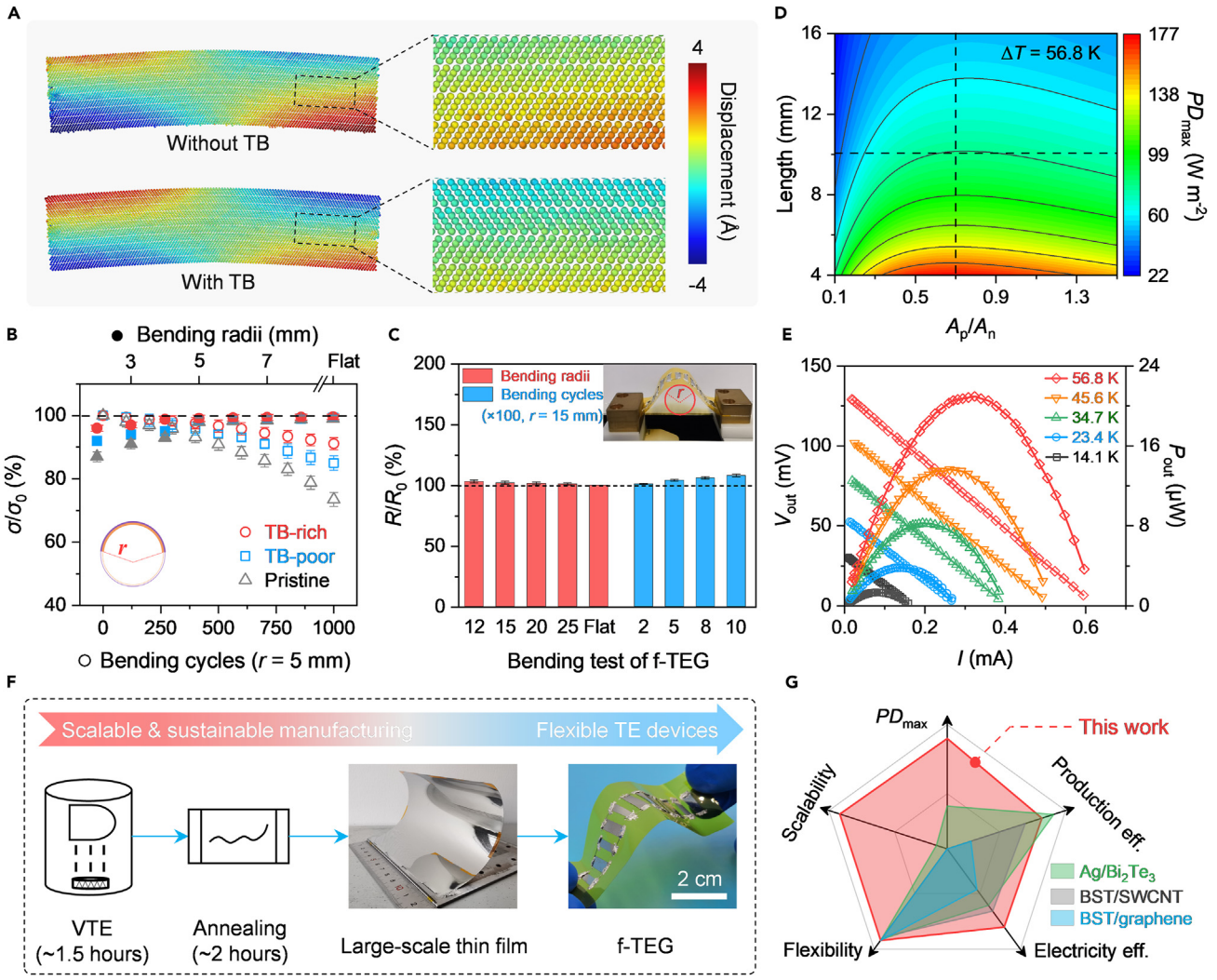


**Figure 5. Scalable and sustainable manufacturing of the flexible $Bi_{0.4}Sb_{1.6}Te_3$ thin films and physics-guided f-TEG**

(A) Molecular dynamics (MD) simulations of the crystal structure without (top) and with (bottom) TB under bending deformation. The models were projected onto the Y-Z plane, with displacements corresponding to tensile and compressive strains along the $<\bar{1}2\bar{1}0>$ direction.

(B and C) Flexible bending tests of BST thin films (B) and (C) the f-TEG. Relative electrical resistance as a function of bending radius (solid pattern) and bending cycles (hollow pattern) for TB-rich, TB-poor, and pristine BST films. $\sigma$ and $\sigma_0$ are the resistances of the samples in the bending deformation state and original flat state, respectively.

(D) Simulated maximum output power density versus geometry, $\Delta T$ = 56.8 K.

(E) Output voltage and power at different temperatures for f-TEG.

(F) Schematic diagram showing the process of preparing BST thin films and f-TEG.

(G) Comparison of sustainable performance between the materials and devices.[9,12,46] The production efficiency was defined as the inverse of the production cycle time for a TE thin film, while the electricity efficiency was defined as the inverse of total electricity consumption during the same production cycle. The precise values for these parameters are listed in Table 1.

temperature, which was competitive with corresponding bulk materials. The TB-rich BST film exhibited a modest variation (<10%) in electrical conductivity after 1,000 bending cycles with a bending radius of 5 mm. We subsequently developed an f-TEG with excellent flexibility and achieved a notable $PD_{max}$ of 69 W m$^{-2}$ under a temperature difference of 56.8 K. These findings may serve as a foundation for future advancements in developing efficient and cost-effective TE devices for sustainable energy applications.

## EXPERIMENTAL PROCEDURES

### BST thin films and f-TEG preparation

Large-scale BST thin films were deposited on a flexible Kapton (PI) substrate using the VTE method, employing commercial BST as the target material. The uniformity of the films was precisely maintained by regulating the vacuum level in the cavity, the substrate-to-target distance, the deposition rate, and ensuring a steady rotational speed of the substrate. This formed the basis for the design and optimization of f-TEG. Additional details are provided in the supplemental information.

**Table 1. Sustainability assessment of the state-of-the-art $Bi_2Te_3$-based thin films**

| TE thin films | Target materials | Methods* | Time cost (h) | Electricity (kWh)* | $CO_2$ emission (kg)* | Scalability | Refs. |
|---|---|---|---|---|---|---|---|
| Ag-doped $Bi_2Te_3$ | Ag, Bi, Te | MS + HP + Ann | ~2 | ~22 | ~15.6 | >11 $cm^2$ | Zheng et al.[12] |
| $Bi_{0.5}Sb_{1.5}Te_3$-SWCNT | $Bi_2Te_3$, $Sb_2Te_3$, Te | CVD (SWCNT) + MS | >3 | >20 | >14.2 | N/A | Jin et al.[9] |
| $Bi_{0.5}Sb_{1.5}Te_3$-graphene | Bi, Sb, Te | CVD (graphene) + PLD | >10 | >30 | >21.3 | ~1 $cm^2$ | Kim et al.[46] |
| $Bi_{0.4}Sb_{1.6}Te_3$ | $Bi_{0.4}Sb_{1.6}Te_3$ | VTE + Ann | 3.5 | ~16 | ~11.4 | large-scale (>100 $cm^2$) | This work |

The electric power of deposition equipment and post-synthesis of the thin films were slightly different in the reports. In our estimations, we assumed an electricity usage of 8 kW for PVD deposition, 3.5 kW for CVD equipment, 15 kW for hot-pressing, and 6 kW for annealing treatments. For equivalent $CO_2$ emissions: 1 kWh electricity = 0.709 kg $CO_2$.[47]

*MS, magnetron sputtering; HP, hot-pressuring; VTE, vacuum thermal evaporation; PLD, pulsed laser deposition; CVD, chemical vapor deposition; Ann, annealing treatment.

### Material characterization

The details can be found in the supplemental information.

### Theoretical calculation and simulation

Density functional theory (DFT) and MD simulations were performed to determine the transport and flexibility mechanisms of TB in the thin films. Finite-element analysis (FEA) was employed to facilitate geometry-dependent optimization for f-TEG. A SPB model was constructed to elucidate the carrier transport performance. Additional details can be found in the supplemental information.

## RESOURCE AVAILABILITY

### Lead contact

Further information and requests for resources and materials should be directed to and will be fulfilled by the lead contact, Jiaqing He (hejq@sustech.edu.cn).

### Materials availability

All materials generated in this study are available from the lead contact on request.

### Data and code availability

The datasets generated during this study are available from the lead contact on reasonable request.

## ACKNOWLEDGMENTS

This research was supported by the National Natural Science Foundation of China (grant no. 11934007), the Science and Technology Innovation Committee Foundation of Shenzhen (grant no. JCYJ20200109141205978), and the Outstanding Talents Training Fund in Shenzhen (202108). We also acknowledge the SEM and TEM resources from the Core Research Facilities at the Southern University of Science and Technology.

## AUTHOR CONTRIBUTIONS

D.M., Y.Z., and J.H. conceived the general idea and designed the experiments. J.H. and G.W.H. supervised the project. D.M. fabricated the samples and devices, characterized their performances and microstructures, and wrote the manuscript. Y.Z. engineered the device testing apparatus, carried out finite-element simulations, and conducted data analysis. Y.Y. performed the TEM section. Y.W. contributed to the DFT calculation. M.H. and J.F. measured the thermal conductivity. Q.M. carried out the MD simulation. Y.L., M.K., Q.G., H.Y., X.X., and L.X. contributed ideas for materials synthesis, characterization, and simulation. All authors discussed and commented on the results.

## DECLARATION OF INTERESTS

The authors declare no competing interests.

## SUPPLEMENTAL INFORMATION

Supplemental information can be found online at https://doi.org/10.1016/j.joule.2024.08.009.

Received: May 5, 2024
Revised: June 13, 2024
Accepted: August 15, 2024
Published: September 12, 2024

## REFERENCES

1. He, J., and Tritt, T.M. (2017). Advances in thermoelectric materials research: looking back and moving forward. Science *357*, eaak9997. https://doi.org/10.1126/science.aak9997.
2. Cao, T., Shi, X.-L., and Chen, Z.-G. (2023). Advances in the design and assembly of flexible thermoelectric device. Prog. Mater. Sci. *131*, 101003. https://doi.org/10.1016/j.pmatsci.2022.101003.
3. Jia, Y., Jiang, Q., Sun, H., Liu, P., Hu, D., Pei, Y., Liu, W., Crispin, X., Fabiano, S., Ma, Y., and Cao, Y. (2021). Wearable Thermoelectric Materials and Devices for Self-Powered Electronic Systems. Adv. Mater. *33*, e2102990. https://doi.org/10.1002/adma.202102990.
4. Jiang, B., Yu, Y., Cui, J., Liu, X., Xie, L., Liao, J., Zhang, Q., Huang, Y., Ning, S., Jia, B., et al. (2021). High-entropy-stabilized chalcogenides with high thermoelectric performance. Science *371*, 830–834. https://doi.org/10.1126/science.abe1292.
5. Zhang, L., Shi, X.L., Yang, Y.L., and Chen, Z.G. (2021). Flexible thermoelectric materials and devices: From materials to applications. Mater. Today *46*, 62–108. https://doi.org/10.1016/j.mattod.2021.02.016.
6. Dong, J., Suwardi, A., Tan, X.Y., Jia, N., Saglik, K., Ji, R., Wang, X., Zhu, Q., Xu, J., and Yan, Q. (2023). Challenges and opportunities in low-dimensional thermoelectric nanomaterials. Mater. Today *66*, 137–157. https://doi.org/10.1016/j.mattod.2023.04.021.
7. Tang, X., Li, Z., Liu, W., Zhang, Q., and Uher, C. (2022). A comprehensive review on $Bi_2Te_3$-based thin films: Thermoelectrics and beyond. Interdiscip. Mater. *1*, 88–115. https://doi.org/10.1002/idm2.12009.

8. Hu, B., Shi, X.-L., Cao, T., Li, M., Chen, W., Liu, W.-D., Lyu, W., Tesfamichael, T., and Chen, Z.-G. (2023). Advances in Flexible Thermoelectric Materials and Devices Fabricated by Magnetron Sputtering. Small Sci. 2300061. https://doi.org/10.1002/smsc.202300061.

9. Jin, Q., Zhao, Y., Long, X., Jiang, S., Qian, C., Ding, F., Wang, Z., Li, X., Yu, Z., He, J., et al. (2023). Flexible Carbon Nanotube-Epitaxially Grown Nanocrystals for Micro-Thermoelectric Modules. Adv. Mater. *35*, e2304751. https://doi.org/10.1002/adma.202304751.

10. Hou, S., Liu, Y., Yin, L., Chen, C., Wu, Z., Wang, J., Luo, Y., Xue, W., Liu, X., Zhang, Q., and Cao, F. (2021). High performance wearable thermoelectric generators using $Ag_2Se$ films with large carrier mobility. Nano Energy *87*, 106223. https://doi.org/10.1016/j.nanoen.2021.106223.

11. Perez-Taborda, J.A., Caballero-Calero, O., Vera-Londono, L., Briones, F., and Martin-Gonzalez, M. (2018). High Thermoelectric *ZT* in n-Type Silver Selenide films at Room Temperature. Adv. Energy Mater. *8*, 1702024. https://doi.org/10.1002/aenm.201702024.

12. Zheng, Z.-H., Shi, X.-L., Ao, D.-W., Liu, W.-D., Li, M., Kou, L.-Z., Chen, Y.-X., Li, F., Wei, M., Liang, G.-X., et al. (2023). Harvesting waste heat with flexible $Bi_2Te_3$ thermoelectric thin film. Nat. Sustain. *6*, 180–191. https://doi.org/10.1038/s41893-022-01003-6.

13. Yang, D., Shi, X.-L., Li, M., Nisar, M., Mansoor, A., Chen, S., Chen, Y., Li, F., Ma, H., Liang, G.X., et al. (2024). Flexible power generators by $Ag_2Se$ thin films with record-high thermoelectric performance. Nat. Commun. *15*, 923. https://doi.org/10.1038/s41467-024-45092-7.

14. Fu, L., Park, K., Kim, S.-I., Kim, B., Song, H.Y., Choi, W., Kim, Y.-M., Hwang, J.-Y., Lee, K.H., and Kim, S.W. (2021). High-Performance Bismuth Antimony Telluride Thermoelectric Membrane on Curved and Flexible Supports. ACS Energy Lett. *6*, 2378–2385. https://doi.org/10.1021/acsenergylett.1c00801.

15. Meng, X., Liu, Z., Cui, B., Qin, D., Geng, H., Cai, W., Fu, L., He, J., Ren, Z., and Sui, J. (2017). Grain Boundary Engineering for Achieving High Thermoelectric Performance in n-Type Skutterudites. Adv. Energy Mater. *7*, 1602582. https://doi.org/10.1002/aenm.201602582.

16. Hu, C., Xia, K., Fu, C., Zhao, X., and Zhu, T. (2022). Carrier grain boundary scattering in thermoelectric materials. Energy Environ. Sci. *15*, 1406–1422. https://doi.org/10.1039/D1EE03802H.

17. Wu, R., Yu, Y., Jia, S., Zhou, C., Cojocaru-Mirédin, O., and Wuttig, M. (2023). Strong charge carrier scattering at grain boundaries of PbTe caused by the collapse of metavalent bonding. Nat. Commun. *14*, 719. https://doi.org/10.1038/s41467-023-36415-1.

18. Kajikawa, Y. (2013). Effects of potential barrier height and its fluctuations at grain boundaries on thermoelectric properties of polycrystalline semiconductors. J. Appl. Phys. *114*, 053707. https://doi.org/10.1063/1.4817243.

19. Shin, H.S., Jeon, S.G., Yu, J., Kim, Y.-S., Park, H.M., and Song, J.Y. (2014). Twin-driven thermoelectric figure-of-merit enhancement of $Bi_2Te_3$ nanowires. Nanoscale *6*, 6158–6165. https://doi.org/10.1039/c4nr00191e.

20. Biswas, K., He, J., Zhang, Q., Wang, G., Uher, C., Dravid, V.P., and Kanatzidis, M.G. (2011). Strained endotaxial nanostructures with high thermoelectric figure of merit. Nat. Chem. *3*, 160–166. https://doi.org/10.1038/nchem.955.

21. Witting, I.T., Chasapis, T.C., Ricci, F., Peters, M., Heinz, N.A., Hautier, G., and Snyder, G.J. (2019). The Thermoelectric Properties of Bismuth Telluride. Adv. Electron. Mater. *5*, 1800904. https://doi.org/10.1002/aelm.201800904.

22. Mamur, H., Bhuiyan, M.R.A., Korkmaz, F., and Nil, M. (2018). A review on bismuth telluride ($Bi_2Te_3$) nanostructure for thermoelectric applications. Renew. Sustain. Energy Rev. *82*, 4159–4169. https://doi.org/10.1016/j.rser.2017.10.112.

23. Li, G., Aydemir, U., Morozov, S.I., Wood, M., An, Q., Zhai, P., Zhang, Q., Goddard, W.A., and Snyder, G.J. (2017). Superstrengthening $Bi_2Te_3$ through nanotwinning. Phys. Rev. Lett. *119*, 085501. https://doi.org/10.1103/PhysRevLett.119.085501.

24. Qin, H., Qu, W., Zhang, Y., Zhang, Y., Liu, Z., Zhang, Q., Wu, H., Cai, W., and Sui, J. (2022). Nanotwins Strengthening High Thermoelectric Performance Bismuth Antimony Telluride Alloys. Adv. Sci. (Weinh) *9*, e2200432. https://doi.org/10.1002/advs.202200432.

25. Mussler, G. (2021). Molecular-Beam Epitaxy of 3D Topological Insulator Thin Films and Devices on Si Substrates. Physica Status Solidi (b) *258*, 2000007. https://doi.org/10.1002/pssb.202000007.

26. Medlin, D.L., Ramasse, Q.M., Spataru, C.D., and Yang, N.Y.C. (2010). Structure of the (0001) basal twin boundary in $Bi_2Te_3$. J. Appl. Phys. *108*, 043517. https://doi.org/10.1063/1.3457902.

27. Yu, Y., He, D.-S., Zhang, S., Cojocaru-Mirédin, O., Schwarz, T., Stoffers, A., Wang, X.-Y., Zheng, S., Zhu, B., Scheu, C., et al. (2017). Simultaneous optimization of electrical and thermal transport properties of $Bi_{0.5}Sb_{1.5}Te_3$ thermoelectric alloy by twin boundary engineering. Nano Energy *37*, 203–213. https://doi.org/10.1016/j.nanoen.2017.05.031.

28. Mao, J., Wang, Y., Kim, H.S., Liu, Z., Saparamadu, U., Tian, F., Dahal, K., Sun, J., Chen, S., Liu, W., and Ren, Z. (2015). High thermoelectric power factor in Cu–Ni alloy originate from potential barrier scattering of twin boundaries. Nano Energy *17*, 279–289. https://doi.org/10.1016/j.nanoen.2015.09.003.

29. Lu, K., Lu, L., and Suresh, S. (2009). Strengthening Materials by Engineering Coherent Internal Boundaries at the Nanoscale. Science *324*, 349–352. https://doi.org/10.1126/science.1159610.

30. Lu, Y., Zhou, Y., Wang, W., Hu, M., Huang, X., Mao, D., Huang, S., Xie, L., Lin, P., Jiang, B., et al. (2023). Staggered-layer-boosted flexible $Bi_2Te_3$ films with high thermoelectric performance. Nat. Nanotechnol. *18*, 1281–1288. https://doi.org/10.1038/s41565-023-01457-5.

31. Shang, H., Dun, C., Deng, Y., Li, T., Gao, Z., Xiao, L., Gu, H., Singh, D.J., Ren, Z., and Ding, F. (2020). $Bi_{0.5}Sb_{1.5}Te_3$-based films for flexible thermoelectric devices. J. Mater. Chem. A *8*, 4552–4561. https://doi.org/10.1039/C9TA13152C.

32. Varghese, T., Dun, C., Kempf, N., Saeidi-Javash, M., Karthik, C., Richardson, J., Hollar, C., Estrada, D., and Zhang, Y. (2020). Flexible Thermoelectric Devices of Ultrahigh Power Factor by Scalable Printing and Interface Engineering. Adv. Funct. Mater. *30*, 1905796. https://doi.org/10.1002/adfm.201905796.

33. Ao, D.-W., Liu, W.-D., Zheng, Z.-H., Shi, X.-L., Wei, M., Zhong, Y.-M., Li, M., Liang, G.-X., Fan, P., and Chen, Z.-G. (2022). Assembly-Free Fabrication of High-Performance Flexible Inorganic Thin-Film Thermoelectric Device Prepared by a Thermal Diffusion. Adv. Energy Mater. *12*, 2202731. https://doi.org/10.1002/aenm.202202731.

34. Wei, M., Shi, X.-L., Zheng, Z.-H., Li, F., Liu, W.-D., Xiang, L.-P., Xie, Y.-S., Chen, Y.-X., Duan, J.-Y., Ma, H.-L., et al. (2022). Directional Thermal Diffusion Realizing Inorganic $Sb_2Te_3$/Te Hybrid Thin Films with High Thermoelectric Performance and Flexibility. Adv. Funct. Mater. *32*, 2207903. https://doi.org/10.1002/adfm.202207903.

35. Lu, Y., Qiu, Y., Cai, K., Ding, Y., Wang, M., Jiang, C., Yao, Q., Huang, C., Chen, L., and He, J. (2020). Ultrahigh power factor and flexible silver selenide-based composite film for thermoelectric devices. Energy Environ. Sci. *13*, 1240–1249. https://doi.org/10.1039/C9EE01609K.

36. Jung, J., Suh, E.H., Jeong, Y.J., Yang, H.S., Lee, T., and Jang, J. (2019). Efficient Debundling of Few-Walled Carbon Nanotubes by Wrapping with Donor–Acceptor Polymers for Improving Thermoelectric Properties. ACS Appl. Mater. Interfaces *11*, 47330–47339. https://doi.org/10.1021/acsami.9b16012.

37. Xu, Q., Qu, S., Ming, C., Qiu, P., Yao, Q., Zhu, C., Wei, T.-R., He, J., Shi, X., and Chen, L. (2020). Conformal organic–inorganic semiconductor composites for flexible thermoelectrics. Energy Environ. Sci. *13*, 511–518. https://doi.org/10.1039/C9EE03776D.

38. Jiang, C., Wei, P., Ding, Y., Cai, K., Tong, L., Gao, Q., Lu, Y., Zhao, W., and Chen, S. (2021). Ultrahigh performance polyvinylpyrrolidone/$Ag_2Se$

composite thermoelectric film for flexible energy harvesting. Nano Energy *80*, 105488. https://doi.org/10.1016/j.nanoen.2020.105488.

39. Kim, K.-C., Lee, J., Kim, B.K., Choi, W.Y., Chang, H.J., Won, S.O., Kwon, B., Kim, S.K., Hyun, D.-B., Kim, H.J., et al. (2016). Free-electron creation at the 60° twin boundary in $Bi_2Te_3$. Nat. Commun. *7*, 12449. https://doi.org/10.1038/ncomms12449.
40. Tan, M., Shi, X.-L., Liu, W.-D., Li, M., Wang, Y., Li, H., Deng, Y., and Chen, Z.-G. (2021). Synergistic Texturing and Bi/Sb-Te Antisite Doping Secure High Thermoelectric Performance in $Bi_{0.5}Sb_{1.5}Te_3$-Based Thin Films. Adv. Energy Mater. *11*, 2102578. https://doi.org/10.1002/aenm.202102578.
41. Lee, H.S. (2016). Thermoelectrics: Design and Materials (John Wiley & Sons, Ltd).
42. Ling, Y., Han, M., Xie, J., Qiu, G., Dong, G., Min, E., Zhang, P., Zeng, X., Liu, R., and Sun, R. (2023). Thermal conductivity measurement of thermoelectric films using transient Photo-Electro-Thermal technique. Measurement *217*, 113058. https://doi.org/10.1016/j.measurement.2023.113058.
43. Ran, Y., Lu, Z., Zhang, X., Li, W., Duan, B., Zhai, P., and Li, G. (2021). The influence of twin boundary on lattice thermal conductivity of thermoelectric InSb. Appl. Phys. Lett. *119*, 161601. https://doi.org/10.1063/5.0068007.
44. Jin, Q., Jiang, S., Zhao, Y., Wang, D., Qiu, J., Tang, D.-M., Tan, J., Sun, D.-M., Hou, P.-X., Chen, X.-Q., et al. (2019). Flexible layer-structured $Bi_2Te_3$ thermoelectric on a carbon nanotube scaffold. Nat. Mater. *18*, 62–68. https://doi.org/10.1038/s41563-018-0217-z.
45. Lu, K. (2016). Stabilizing nanostructures in metals using grain and twin boundary architectures. Nat. Rev. Mater. *1*, 16019. https://doi.org/10.1038/natrevmats.2016.19.
46. Kim, E.S., Hwang, J.-Y., Lee, K.H., Ohta, H., Lee, Y.H., and Kim, S.W. (2017). Graphene Substrate for van der Waals Epitaxy of Layer-Structured Bismuth Antimony Telluride Thermoelectric Film. Adv. Mater. *29*, 1604899. https://doi.org/10.1002/adma.201604899.
47. Zhou, Y., Liu, X., Jia, B., Ding, T., Mao, D., Wang, T., Ho, G.W., and He, J. (2023). Physics-guided co-designing flexible thermoelectrics with techno-economic sustainability for low-grade heat harvesting. Sci. Adv. *9*, eadf5701. https://doi.org/10.1126/sciadv.adf5701.
48. Shi, X., Chen, H., Hao, F., Liu, R., Wang, T., Qiu, P., Burkhardt, U., Grin, Y., and Chen, L. (2018). Room-temperature ductile inorganic semiconductor. Nat. Mater. *17*, 421–426. https://doi.org/10.1038/s41563-018-0047-z.
49. Pang, K., Miao, L., Zhang, Q., Pan, Q., Liu, Y., Shi, H., Li, J., Zhou, W., Zhang, Z., Zhang, Y., et al. (2024). Gradient Nanotwins and Enhanced Weighted Mobility Synergistically Upgrade $Bi_{0.5}Sb_{1.5}Te_3$ Thermoelectric and Mechanical Performance. Adv. Funct. Mater. *34*, 2315591. https://doi.org/10.1002/adfm.202315591.
50. Jia, F., Wu, R., Liu, C., Lan, J., Lin, Y.-H., and Yang, X. (2019). High Thermoelectric and Flexible PEDOT/SWCNT/BC Nanoporous Films Derived from Aerogels. ACS Sustainable Chem. Eng. *7*, 12591–12600. https://doi.org/10.1021/acssuschemeng.9b02518.
51. Liu, J., Jia, Y., Jiang, Q., Jiang, F., Li, C., Wang, X., Liu, P., Liu, P., Hu, F., Du, Y., and Xu, J. (2018). Highly Conductive Hydrogel Polymer Fibers toward Promising Wearable Thermoelectric Energy Harvesting. ACS Appl. Mater. Interfaces *10*, 44033–44040. https://doi.org/10.1021/acsami.8b15332.